日本磁気学会
ISSN 2432-0250
Journal of the Magnetics Society of Japan
Electronic Journal URL: https://www.jstage.jst.go.jp/browse/msjmag

Vol.46 No.4　2022

Journal

JOURNAL OF THE MAGNETICS SOCIETY OF JAPAN

Vol.46 No.4 2022

日本磁気学会

ISSN 2432-0250

HP: http://www.magnetics.jp/ e-mail: msj@bj.wakwak.com

Electronic Journal: http://www.jstage.jst.go.jp/browse/msjmag

Journal of the Magnetics Society of Japan
Vol. 46, No. 4

Electronic Journal URL: https://www.jstage.jst.go.jp/browse/msjmag

CONTENTS

J. Magn. Soc. Jpn., **46**, 76-84 (2022)

<Review>

Microstructure control for magnetic thin films with high functionality

Y.K. Takahashi
National Institute for Materials Science, *1-2-1 Sengen, Tsukuba, 305-0047, Japan*

In most magnetic devices with thin films, the magnetic properties are governed by not only the intrinsic properties but also the microstructure. To realize high performance in magnetic devices, understanding the correlation between magnetic properties and microstructure is important. In this study, the development of ferromagnetic thin films for high-density recording media and large output current perpendicular to plane giant magnetoresistance devices are reviewed. Based on the experimental data, the research direction for next-generation high-areal-density magnetic recording is discussed.

Key words: magnetic recording, microstructure, thin film

1. Introduction

In this article, several research topics for the MSJ Achievement Award 2021 are introduced. In many magnetic functional materials and devices, intrinsic properties as well as extrinsic properties, such as coercivity, which strongly depend on the microstructure, are used as important parameters. To improve the performance of such materials and devices, it is necessary to appropriately control the microstructure. Here, the author introduces her work on FePt media for heat-assisted magnetic recording (HAMR) in hard disk drives (HDDs), and current-perpendicular-to-plane giant magnetoresistance (CPP-GMR) devices using Co-based Heusler alloys.

The representative device for magnetic recording is the HDD, which has the three advantages of large capacity, low cost, and non-volatility, and is expected to continue to increase in density as a key technology supporting Society 5.0. The basic structure has not changed since the first HDD, RAMAC, which is a large device with the size of two refrigerators, with disks approximately 60 cm in diameter and weighing over one ton, but with a small storage capacity of 4.4 MB. If the capacity of a HDD in a standard PC today is approximately 1 TB, this indicates that the storage capacity has increased 200 million-fold over the past 60 years. Figure 1 shows the evolution of HDD recording density, along with technological innovations in the media and reader (the inset shows the vertical axis on a linear scale). Important technological innovations include the introduction of AMR heads using the anisotropic magnetoresistance effect in 1991, GMR[1)] heads using the giant magnetoresistance effect in 1998, and tunneling magnetoresistance (TMR) heads in 2004. While inductive heads function as magnetic sensors using induced electromotive force, AMR, GMR, and TMR heads are magnetic sensors that convert an external magnetic field into a change in resistance. For the AMR effect, which was discovered by Lord Kelvin in 1857, the electrical resistance between terminals AB attached to a magnet changes when a magnetic field is applied, as shown in Figure 2(a). This works as a magnetic sensor using the change in the magnetic domain structure due to the application of a magnetic field or, in a device with a single domain, the electrical conduction that depends on the relative angle between the magnetization and the terminals AB. The change in the electrical resistance is only 1–2% at most, and a magnetic sensor with higher sensitivity is required for HDD applications. The GMR sensor consists of a magnet and a nonmagnetic metal (NM in the figure), as shown in Figure 2(b), while the TMR sensor consists of a magnet and a non-magnetic insulator (NI in the figure), as shown in Figure 2(c). Generally, the change in the relative magnetization configuration of the magnets separated by a nonmagnetic metal or a nonmagnetic insulator appears as a change in the electrical resistance between terminals AB. If the coercive force of one magnet is made strong and adjusted such that only the other magnet changes its magnetization direction in response to an applied magnetic field, it can act as a magnetic sensor. Figure 1 shows that recording density increased tremendously in the 1990s, largely due to successive technological innovations in readers, such as AMR, GMR, and

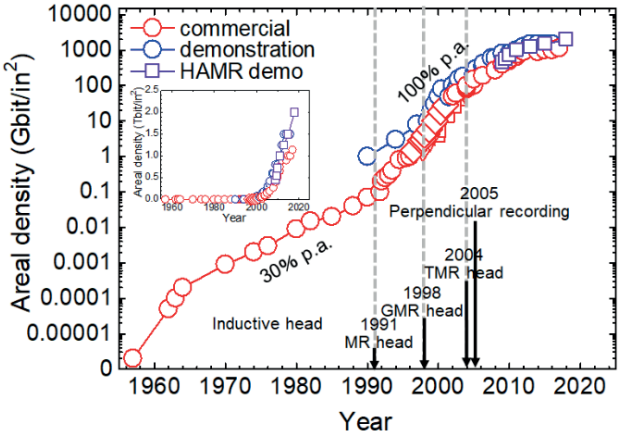

Fig. 1 Evolution of HDD recording density along with technological innovations in the media and reader.

Y.K. Takahashi, takahashi.yukiko@nims.go.jp

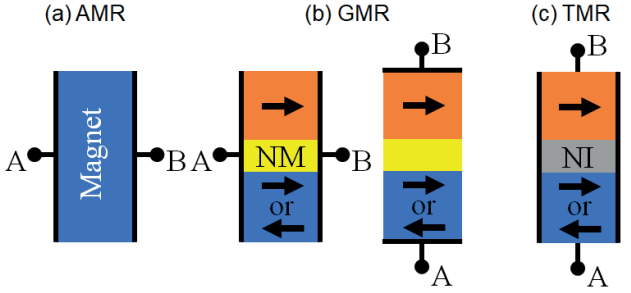

Fig. 2 Schematic views of (a) AMR sensor, (b) GMR sensor and (c) TMR sensor.

TMR heads. As for media, the shift from longitudinal magnetic recording to perpendicular magnetic recording[2] in 2005 was an important technological innovation.

The directions of magnetization of the nanomagnets that make up the media are longitudinal and perpendicular. In longitudinal magnetic recording, the stray field between adjacent magnetic domains corresponds to the magnetic bits, whereas in perpendicular magnetic recording, the magnetic domains correspond to the magnetic bits. To achieve a high areal density, the area per bit must be reduced, but simultaneously, the size of the ferromagnetic grains that constitute the nanomagnets must be reduced. Noise generated by the medium mainly originates from the transition region between bits and achieves a transition region should be as smooth as possible, leading to a sharp magnetization transition and noise reduction. If the direction of magnetization is oriented in-plane, the magnetization will point in opposite directions at the transitions will occur in some places. Consequently, a larger demagnetizing field is generated at the center of the magnetization transition region, which causes the magnetization to decay and the magnetization transition to become wider. The higher the recording density, that is, the smaller the bit size, the greater the effect of this demagnetization field, and the longitudinal recording reaches its limit at approximately 200 Gbit/in^2. To further increase the recording density, it is necessary to switch to perpendicular magnetic recording, where the demagnetization field stabilizes the nanomagnet. Furthermore, TMR devices were developed to replace the current-in-plane (CIP)-GMR device, in which the current flows in the in-plane direction in an all-metal multilayer of ferromagnetic metal/nonmagnetic metal/ferromagnetic metal, with a nonmagnetic insulator MgO, and to utilize the tunnel conduction of electrons with the current flowing in the perpendicular direction to the film plane[3,4]. The TMR device exhibited a magnetoresistance ratio of over 100% and supported a high rate of increase in recording density for some time thereafter.

However, the growth in areal density slowed around the year 2010. A high areal density requires greater magnetic anisotropy to maintain the direction of the magnetization that is responsible for the recorded information in the finer nanomagnets. However, the magnetic field that can be generated by the write head has already reached its upper limit, and the current perpendicular magnetic recording (PMR) can no longer handle the magnetic field control of media with high magnetic anisotropy. Even under these circumstances, density has gradually increased through the adoption of shingled magnetic recording (SMR), a mechanism that stores data while overlapping portions of the media to write a narrower width than the conventional write head.

To achieve high-density HDDs, refinement of the microstructure in magnetic recording media is essential. If the CoCrPt alloy, the current media material, is further refined, the anisotropy energy of the grains becomes comparable to the thermal energy, causing a stochastic magnetization reversal. To solve this thermal agitation problem, it is necessary to use a highly anisotropic material as the medium. However, when the grain size of highly anisotropic materials is refined, the external magnetic field required for magnetization reversal becomes several Tesla, making writing impossible using current recording devices. The inability to simultaneously satisfy the three requirements of high density (refined microstructure), reliability (thermal stability), and writability (magnetization reversal field) is called the trilemma problem. Energy-assisted magnetic recording, in which magnetization reversal is assisted by external energy during writing, has been proposed to solve this trilemma problem. External assist energy includes heat, high-frequency magnetic fields, and light. Heat-assisted magnetic recording (HAMR), which uses heat, was shipped to data centers by Seagate in the United States in December 2020 and is currently in practical use.

In this review article, the author introduces the development of FePt media for heat-assisted magnetic recording and CPP-GMR sensors for next-generation devices.

2. Microstructure control for magnetic thin films with high functionality

2.1 Recording media for heat-assisted magnetic recording

Microstructure Control of FePt Granular Thin Films

FePt with an $L1_0$ ordered structure has a large magnetocrystalline anisotropy of 7 MJ/m^3 [5] and has been attracting attention as a material for next-generation magnetic recording media since around 2000, when the 1 Tbit/in^2 barrier was in sight. However, microstructure control was difficult, and there were no thoughts that a medium using FePt would be realized at that time. First, the difficulty in controlling the microstructure of FePt is explained. The phase diagram of FePt is shown in Figure 3[6]. Although there is a wide composition region that assumes the $L1_0$ structure, the target composition as a medium material is FePt with a ratio of 1:1 because magnetocrystalline anisotropy is maximized at a 1:1 composition. The phase diagram shows that the driving force for ordering is high because the order-disorder transformation temperature of FePt is high at 1300 °C. In bulk experiments, ordering cannot be stopped when the FePt alloy quenches from the high-temperature disordered phase[7]. However, the sputtering method used to fabricate the media is a gas-phase quenching method; therefore, the disordered phase is formed immediately after deposition.

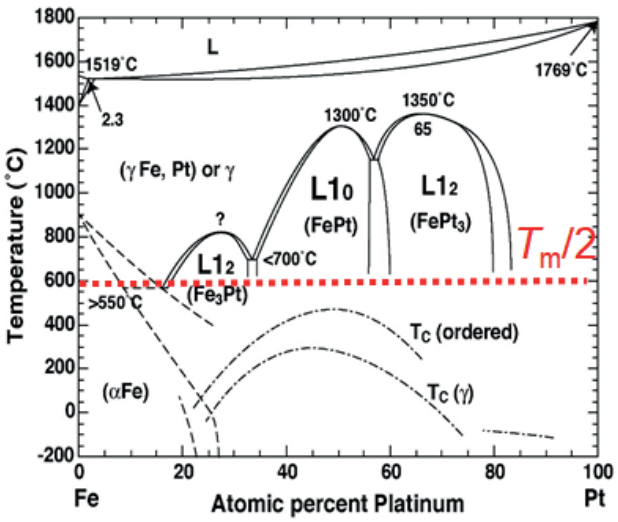

Fig. 3 Phase diagram of Fe-Pt binary alloy[6]. T_m stands for melting temperature.

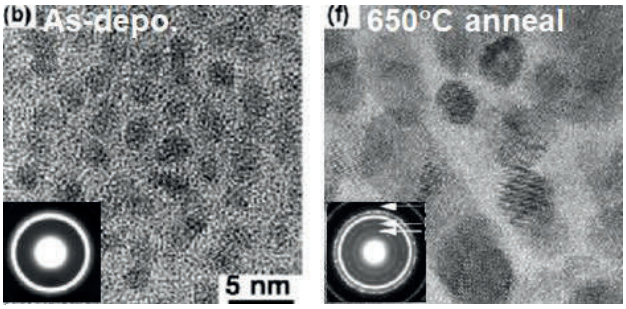

Fig. 4 Microstructures and selected area electron diffraction patterns of (b) as-deposited. and (f) after annealing at 650°C in FePt-Al_2O_3 granular film. (Reproduced from *Appl. Phys. Lett*., **76**, 3971 (2000) with permission of American Institute of Physics).

Because the magnetocrystalline anisotropy of the disordered phase is small, it is necessary to order it by annealing from the disordered phase of A1 to the ordered phase of $L1_0$ to use it as a medium. Annealing higher than half the melting temperature (T_m in Fig. 3) is required when volume diffusion is used for ordering. For FePt, the temperature was as high as 600 °C. When heat-treated at such a high temperature, as shown in Figure 4, the average grain diameter immediately after deposition is approximately 2 nm; however, after heat treatment, the grains coalesce, and the grain diameter becomes larger. The difficulty in controlling the microstructure of FePt lies in the compatibility of fine grains several nanometers in size and the high-temperature process for ordering[8].

Research on the application of $L1_0$-FePt to media has increased since 2000. The main approach was to fabricate granular FePt thin films using various nonmagnetic matrix materials and evaluate their magnetic properties. Coercivity is an important property of magnetic recording media and is strongly dependent on the microstructure. To obtain a high coercivity, it is important to combine not only magnetic property evaluation

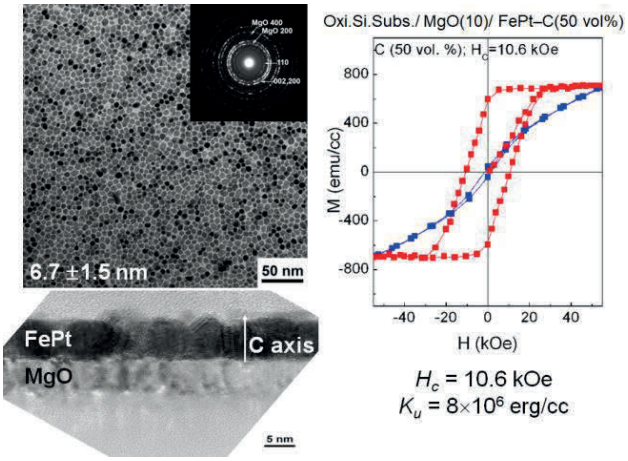

Fig. 5 (a) in-plane bright-field TEM image and selected area electron diffraction pattern, (b) cross-sectional bright-field TEM image, (c) out-of-plane and in-plane magnetization curves of FePt-C granular films deposited on thermally oxidized Si substrate. (Reproduced from *Appl. Phys. Express* **1**, 101301 (2008) with permission of The Japan Society of Applied Physics).

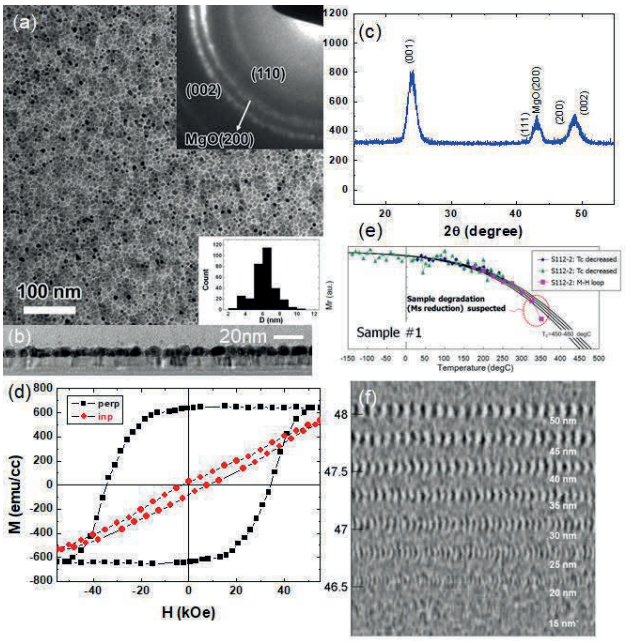

Fig. 6 (a) in-plane bright-field TEM image and selected area electron diffraction pattern, (b) cross-sectional bright-field TEM image, (c) XRD pattern, (d) out-of-plane and in-plane magnetization curves, (e) temperature dependence of magnetization and (f) Recording pattern tracks written at various bit lengths from 15 to 50 nm. The track width is 92 nm in FePtAg-C granular films deposited on thermally oxidized Si substrate.

but also microstructure observation. Therefore, FePt media was fabricated with various nonmagnetic matrices, the mechanism of coercivity by microstructure observation was investigated, and the findings were fed back to the process to achieve high coercivity. While observing the microstructures of the fabricated samples, it was observed that phase separation of FePt-C occurred in the film growth direction, whereas most FePt granular films showed phase separation only in the in-plane direction. This indicates that FePt and C exhibit a strong phase separation tendency. Subsequently, by optimizing the sputtering conditions, we succeeded in fabricating a sample with an average grain size of approximately 6 nm, a narrow grain size distribution, and perpendicular magnetic anisotropy, as shown in Figure 5[9]. Because the substrate temperature was set relatively low at 400 °C to suppress grain coalescence, the degree of order was approximately 0.6, and the coercivity was 10 kOe (1 T), which was not as high as expected from the magnetocrystalline anisotropy. When a small amount of Ag was added to the FePt-C granular film, the degree of order increased while maintaining a uniform microstructure, and an extremely high coercivity of 35 kOe (3.5 T) was successfully achieved (Figure 6) [10,11]. Ag addition increases the degree of order. Later, TEM-EDS observations of Ag-doped FePt-C granular thin films showed that Ag precipitated around the FePt grains, forming a Ag/FePt core-shell structure[12]. In other words, Ag supersaturated by sputtering is considered to have increased the degree of order because of the replacement of atoms in the rejection process because Ag and FePt are immiscible. Static write tests on this FePt medium at HGST's San Jose Research Center reached 550

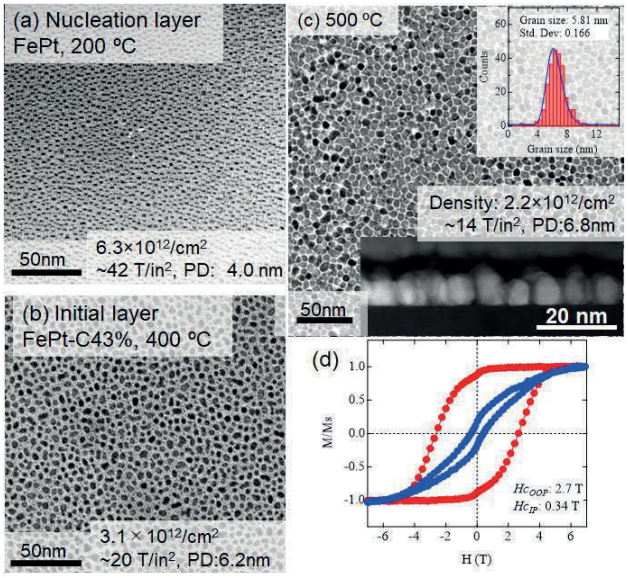

Fig. 7 Bright-field in-plane TEM images of (a) a nucleation layer, (b) an initial layer and (c) after deposition of a main layer, and (d) out-of-plane and in-plane magnetization curves of FePt-C granular film prepared by 3-step deposition method. (Reproduced from *J. Magn. Magn. Mater.* **500**, 166418 (2020) with permission of ELSEVIER).

Gbit/in^2, the highest recording density in HAMR at that time in 2011 was achieved[11]. This announcement triggered an acceleration of research and development for the practical application of FePt recording media.

Although successful in fabricating a sample with both microstructure and magnetic properties that could be useful as a medium, there were many challenges to overcome before it could be used in devices. For the media, these include further refinement of the grain size[13], formation of a columnar structure[14], development of a conductive substrate[15], reduction of in-plane hysteresis[16], and suppression of distributions. The author's group has provided material science guidelines for each of these issues through joint research with manufacturers.

To achieve 4 Tbit/in^2, a columnar structure with an average grain size of less than 4 nm, a grain pitch of less than 5 nm, a grain density of more than 25 Tgrains/in^2, a grain size distribution of less than 15%, and an aspect ratio of more than 1.5 are required[17]. A high degree of ordering is required, too. Therefore, a three-step deposition method[13], which consists of a nucleation layer, initial layer, and main layer, was introduced; the FePt recording layer was fabricated in a one-step process. The process was optimized to maximize the grain density in each layer and achieve a high degree of order. The microstructure of the FePt-C granular film fabricated under optimal conditions is shown in Figure 7(c). The average grain size was approximately 5.8 nm and the grain density was 14.2 Tgrains/in^2. As shown in Figure 7(a), the nucleation layer showed a high grain density of 41.9 Tgrains/in^2, but the grain density was reduced by depositing the initial and main layers. This is thought to cause the coalescence of grains with increasing film thickness, resulting in an increase in grain size and a reduction in grain density. The magnetization curve of this sample is shown in Figure 7(d). It shows high perpendicular anisotropy and a perpendicular coercivity of 2.7 T was obtained.

Although a three-step deposition method was introduced, as long as C is used as a single nonmagnetic matrix material, a high density of 4 Tbit/in^2 cannot be achieved. FePt-Cr_2O_3 was applied to the three-step deposition method, known from previous studies, to produce finer grains and a columnar structure. The results of microstructure optimization are shown in Figure 8[18]. The microstructure showed average grain size of 4.28 nm, a grain pitch of 5.2 nm, and a grain density of 24 T/in^2, which corresponds to the microstructure of a 4 Tbit/in^2 media. However, the degree of order and perpendicular anisotropy were low. Figure 9 shows an EDS map of the sample. At first glance, FePt and Cr seem to be separated, but the interface between Fe and Cr is blurred, while the interface between Pt is clear. This implies that Fe diffused into the Cr-O matrix, and Cr diffused into the FePt particles. Other studies have shown that Cr diffusion into FePt grains occurs approximately 1 nm from the FePt surface, which may be the cause of the reduced ordering of the FePt grains. No material has yet been found that provides both high-density grains and a high degree of ordering.

In December 2020, Seagate shipped FePt-HAMR media to data centers, leading to its commercialization. The progression

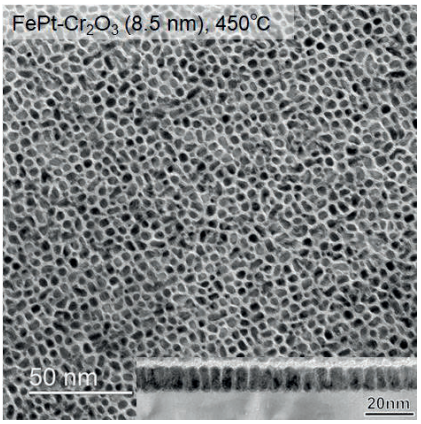

Fig. 8 In-plane bright-field image of FePt-Cr_2O_3 granular film. The inset shows the cross-sectional bright-field TEM image. Total film thickness is 8.5 nm and the deposition temperature is 450°C.

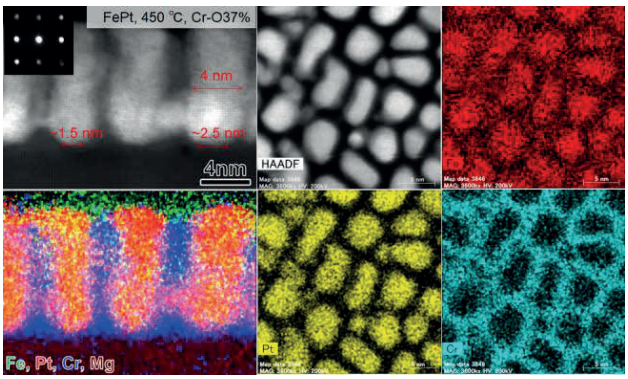

Fig. 9 Cross-sectional and in-plane High-angle Annular Dark Field Scanning TEM (HAADF-STEM) images and corresponding elemental maps.

to the practical application of FePt media is as follows: around 2000, when the 1 Tbit/in^2 barrier began to be observed in current CoCrPt media, basic research began on the use of FePt as a next-generation magnetic recording media material. Around this time, the author also began research on FePt and investigated its ordering process using a transmission electron microscope. At that time, the size effect of ordering in FePt was discovered[19]. Subsequently, in 2008, the author succeeded in synthesizing the world's first FePt-C granular thin film with an extremely uniform microstructure and an average grain size of 6 nm[9]. Furthermore, by adding Ag, the ordering of the FePt grains increased and a high coercivity of 3.5 T was achieved[10]. Using this thin film, the HGST San Jose Research Center conducted a drag test and achieved 550 Gbit/in^2, the highest recording density for HAMR media[11]. Subsequently, the author developed Mg-Ti-O as an alternative material for the MgO underlayer[15], realized FePt grains with a columnar structure using the C-graded deposition method[14], and increased the density by layering different non-magnetic matrix materials and adopting the three-step deposition method[13]. In 2016, Seagate demonstrated 1.5 Tbit/in^2 in actual equipment; in 2017, the company shipped samples of FePt-HAMR media to IT companies, such as Google and Facebook; in December 2020, the product was shipped to data centers for commercialization. The FePt-HAMR medium that has been commercialized does not have the recording density to realize its potential, and meanwhile, R&D will be conducted to achieve 4 Tbit/in^2. The issue with HAMR is the loss of reliability owing to heating during writing. The realization of highly efficient magnetization reversal with the minimum necessary assist energy is urgently required. To this end, it is necessary to understand and control the magnetization reversal of FePt grains. To observe the magnetization dynamics of FePt granular thin films, a 7 T magnetic field and temperature-tunable time-resolved magneto-optical Kerr effect measurement system was set up. The author is currently in the process of gaining insights into these dynamics.

Controlling Magnetization Reversal with Circularly Polarized Light in FePt Media

When using FePt as a magnetic recording medium, an extremely large reversal field of over 3 T exceeds the magnetic field generated by the currently used write head. To solve this problem, energy-assisted magnetization switching, in which magnetization reversal is assisted by external energy, has been proposed. The method in which a laser is used to raise the temperature of the FePt media to near the Curie point during writing is called HAMR and is a type of energy-assisted magnetization reversal. In addition, microwave-assisted magnetic recording (MAMR), in which a high-frequency magnetic field with a frequency close to the ferromagnetic resonance of the medium is applied to resonantly amplify the precession of magnetization and assist in magnetization reversal, has been studied, mainly in Japan. Although still in the proof-of-principle stage compared to HAMR and MAMR, magnetization reversal using circularly polarized light is being investigated. The discovery of magnetization reversal by circularly polarized light is relatively recent: in 2007, Stanciu *et al*. discovered this phenomenon using the ferrimagnetic material GdFeCo[20]. The origin of magnetization reversal by circularly polarized light has been suggested to be due to because of the difference in the decay time of magnetization between transition metals and rare earth metals[21,22] due to MCD[23] and the inverse Faraday effect[24]. Magnetization reversal by circularly polarized light in ferromagnetic materials was first reported by Stephane *et al*. for Co thin films with a synthetic antiferromagnetic film[25]. Subsequently, in 2014, magnetization reversal was demonstrated by circularly polarized light in granular FePt thin films, as shown in Figure 10[26]. The ability to induce magnetization reversal according to the helicity of light in FePt granular films with a coercivity exceeding 3 T without the application of an external magnetic field had a strong impact on the magnetic recording community, which faces technical challenges to generate largest magnetic fields. Subsequent research has revealed that magnetization reversal by circularly polarized light in FePt granular thin films is not a single-pulse event, but an accumulative reversal in which the magnetization is reversed stepwise by multiple laser pulses[26]. The principle of magnetization reversal has been well explained by MCD. This cumulative magnetization reversal is not a phenomenon unique to FePt granular thin films; it also occurs in CoPt-based thin films on a similar principle[27].

To use magnetization reversal using circularly polarized light as a practical technology, it is necessary to achieve magnetization reversal in a single pulse. Therefore, the single-pulse switching of ferromagnetic thin films was experimented using exchange coupling[28]. The prepared thin film was a $[Co/Pt]_4$/Ru/GdFeCo trilayer in which the thickness of Ru was varied to control the exchange coupling between the Co/Pt and GdFeCo layers. Figure 11(a) shows the change in the exchange coupling between the Co/Pt multilayer and the GdFeCo film as a function of Ru thickness; when the Ru is thin, the exchange coupling is antiferromagnetic, but when the Ru thickness is greater than 0.9 nm, the coupling becomes ferromagnetic. Figure 11(b) shows the magnetization reversal

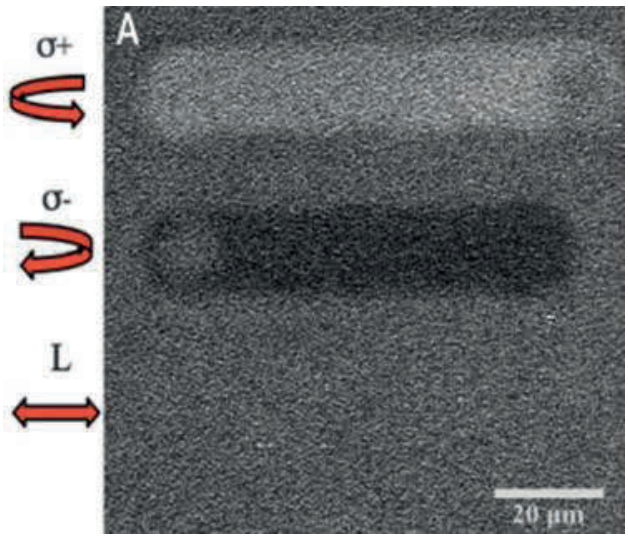

Fig. 10 Magnetic images after scanning the femto-second laser with two different circularly polarized light and linearly polarized light in FePt-C granular sample. The coercivity of the sample is about 3.5 T[26].

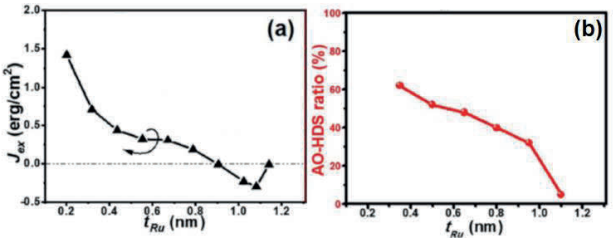

Fig. 11 Interlayer exchange coupling modulated AO-HDS in the [Co/Pt]$_4$/Ru (tRu)/GdFeCo multilayer. (a) The plot of the IEC energy density, J_{ex} and (b) the AO-HDS ratio as a function of the Ru spacer layer thickness. (Reproduced from *J. Phys.D:Appl. Phys.***53**, 475002 (2020) with permission of Institute of Physics, UK).

ratio for a single pulse. The reversal ratio in a single pulse for the [Co/Pt]$_4$ multilayer, which was 14% in a single pulse, increased to 62% when antiferromagnetically exchange coupled with GdFeCo. The magnetization reversal ratio decreased rapidly when the exchange coupling between [Co/Pt]$_4$ and GdFeCo changed from antiferromagnetic to ferromagnetic. This indicates that exchange coupling can be used to increase the magnetization reversal ratio in a single pulse. The origin of this phenomenon is currently being investigated.

2.2 CPP-GMR and nonlocal spin valves using highly spin-polarized Co-based Heusler alloys for hard disk drives (HDDs)

As mentioned in the Introduction, the currently used read sensors are TMR devices that utilize the tunneling magnetoresistance effect. However, TMR devices use MgO insulator spacers, which increase device resistance and make it difficult to support even higher readout speeds in the future. According to Valet and Fert, the area resistance change (ΔRA, R, and A represent the resistance and area of a device) of the CPP-GMR device can be described by the following equation[29]:

$$\Delta RA \approx 2\beta^2\rho_F^* t_F + 4\gamma^2 AR_{F/N}^*, \qquad (1)$$

where β and γ are the spin polarizations of the ferromagnetic electrode material and the interface between the ferromagnetic electrode material and nonmagnetic metal spacer, respectively. It can be observed that the use of a material with high spin polarization is effective in obtaining a high output signal of ΔRA. Because its application is being considered as a read device, the ferromagnetic electrode material must have not only a high spin polarization but also a Curie point sufficiently higher than room temperature (RT). Therefore, this study focused on Co-based Heusler alloys.

Co-based Heusler alloys have an ordered structure of L2$_1$, represented by X$_2$YZ, as shown in Figure 12. However, when

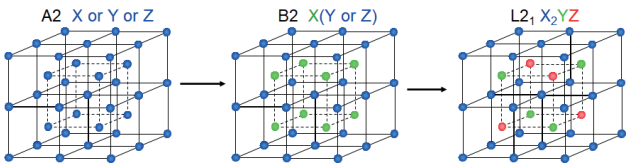

Fig. 12 schematic view of Co-based Heusler alloy with A2, B2 and L2$_1$ ordered structure.

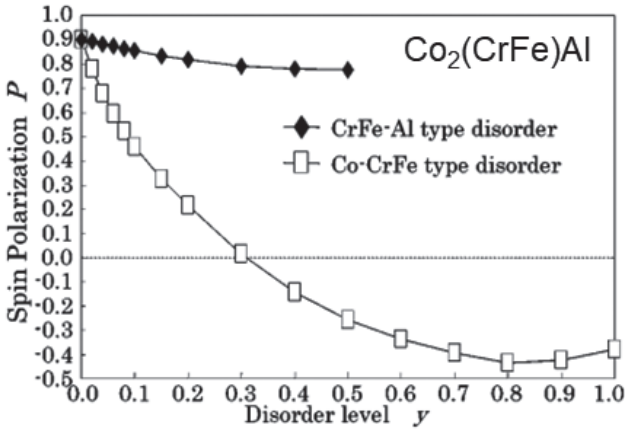

Fig. 13 Changes of spin polarization as a function of disordering level. (Reproduced from *J. Appl. Phys.*, **95**, 7225 (2004) with permission of American Institute of Physics).

thin films are prepared by sputtering, it is difficult to obtain a perfect L2$_1$ structure, and a B2 structure in which Y and Z are disordered or an A2 structure in which all X, Y, and Z atoms are disordered can easily be obtained. As shown in Figure 13, the B2-type disorder (CrFe-Al type disorder in Fig. 13) does not cause a significant decrease in spin polarization, whereas the A2-type disorder (Co-CrFe type disorder in Fig. 13) significantly decreases spin polarization[3]. In other words, it can be observed that an ordered structure with at least a B2 structure is required to obtain a high spin polarization. Furthermore, if the Fermi level (E_F) is in the center of the band gap, the spin polarization reduction is less affected by an increase in the density of states at the band edge owing to disorder or heat. As shown in Figure 14, the E_F in Co$_2$FeAl is at the edge of the valence band, while in Co$_2$FeSi it is at the edge of the conduction band; it can be observed that replacing Al with Si, which has a valence electron number one greater than Al, can move the E_F to the center of the band gap. Spin polarization was also found to be the largest for Co$_2$FeAl$_{0.5}$Si$_{0.5}$[31-35]. From the above, the guideline for material search is to control E_F by varying the valence electron number by adding a fourth element to Co-based Heusler alloys, and to search for a material that can maintain high spin polarization even if a disordered structure is introduced.

Bulk alloys were prepared by arc melting, and spin polarization was measured using the point contact Andreev reflection (PCAR) method along with structural analysis and

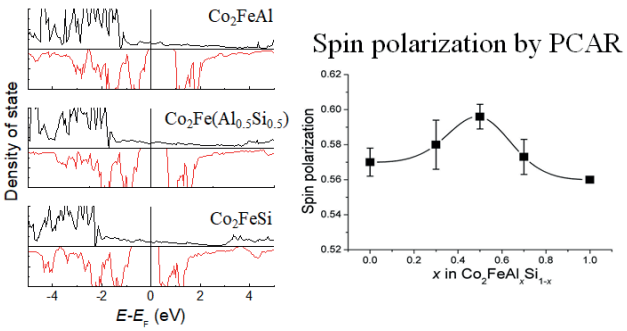

Fig. 14 (a) Density of states in Co$_2$FeAl, Co$_2$Fe(Al$_{0.5}$Si$_{0.5}$) and Co$_2$FeSi and (b) change of spin polarization in Co$_2$FeAl$_x$Si$_{1-x}$. (Reproduced from *J. Appl. Phys.*, **102**, 033916 (2007) with permission of American Institute of Physics).

Table 1 Spin polarization of quaternary, ternary and binary alloys.

Quaternary alloys	P	Ref.
$Co_2Mn(Ge_{0.75}Ga_{0.25})$	74	36
$Co_2Mn(Ga_{0.5}Sn_{0.5})$	72	37
$Co_2Fe(Si_{0.75}Ge_{0.25})$	70	38
$Co_2Fe(Ga_{0.5}Ge_{0.5})$	69	39
$Co_2(Cr_{0.02}Fe_{0.98})Ga$	67	40
$Co_2MnGeSn$	67	41
$Co_2(Mn_{0.95}Fe_{0.05})Sn$	65	42
$(CoFe)_2MnGe$	65	43
$Co_2(Mn_{0.5}Fe_{0.5})Ga$	65	44
$Co_2(Cr_{0.02}Fe_{0.98})Si$	65	45
$Co_2MnTiSn$	64	46
$Co_2MnAl_{0.5}Sn_{0.5}$	63	47
$Co_2MnGa_xSi_{1-x}$	63	48
$Co_2FeAlGa$	63	49
$Co_2MnSiGe$	63	50
$Co_2(Mn_{0.5}Fe_{0.5})Si$	61	51
$Co_2CrFeAl$	60	52
$Co_2Mn(Al_{0.5}Si_{0.5})$	60	53
$Co_2FeGa_{0.5}Si_{0.5}$	60	54
$Co_2Fe(Al_{0.5}Si_{0.5})$	60	34

Ternary alloys	P	Ref.
Co_2MnSi	56	55
Co_2MnGe	58	36
Co_2MnSn	60	47
Co_2MnAl	60	47
Co_2MnGa	60	36
Co_2CrAl	62	52
Co_2FeAl	59	52
Co_2FeSi	60	45
Co_2FeGa	58	56
Co_2CrGa	61	57
Co_2TiSn	57	58
Co_2VAl	48	59
Fe_2VAl	56	59

Metals and binary	P	Ref.
Fe	46	
Co	45	
FeCo	50	
$Co_{75}Fe_{25}$	58	
B2-FeCo	60	
$[Co/Pd]_n$	60	
Fe_4N	59	60
Co/Pt	56	61

magnetic measurements. The results are summarized in Table 1[34-60]. The spin polarization of ternary Co-based Heusler alloys is as high as 62% for Co_2CrAl, whereas Heusler alloys with the addition of a fourth element exhibit spin polarization as high as 74%. Among these, the $Co_2Fe(Ga_{0.5}Ge_{0.5})$ alloy (CFGG), which exhibited a spin polarization of 69%, was used in CPP-GMR devices[62] and nonlocal spin valve devices[63].

Figure 15 shows the layer stack of the CPP-GMR device. Cr (10 nm)/Ag (100 nm) was deposited as an underlayer on a MgO (001) single-crystal substrate, and CFGG/Ag/CFGG, the main part of the CPP-GMR device, was deposited at RT. CFGG/Ag/CFGG epitaxial growth was observed at the upper Ag/CFGG interface with only one misfit dislocation, and all other regions were consistent. The orientation relationship between CFGG and Ag was CFGG(100)[110]//Ag(100)[100]. The nanobeam electron diffraction images shown in Figures 16 (b) and (c) indicate that both the upper and lower CFGGs had a B2 ordered structure. The magnetoresistance curves are shown in Figure 16(e). When the magnetization of the upper and lower CFGG layers is antiparallel, the resistance is high, whereas when the magnetization is parallel, the resistance is low. At RT, the ΔRA is as high as 9.5 mΩ·μm and the magnetoresistance (MR) ratio is 41.7%. To estimate the spin polarization of CFGG, CPP-GMR devices with CFGG layers of different thicknesses were prepared. Figure 16(f) shows a plot of ΔRA versus thickness. The ΔRA increased with thickness up to 5 nm and then became saturated. Fitting this with the Valet and Fert

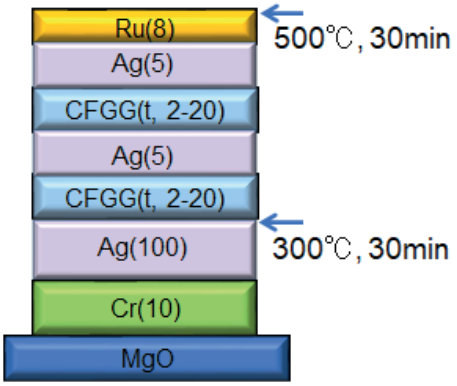

Fig. 15 Schematic view of the film stack for CPP-GMR with CFGG as a ferromagnetic electrode.

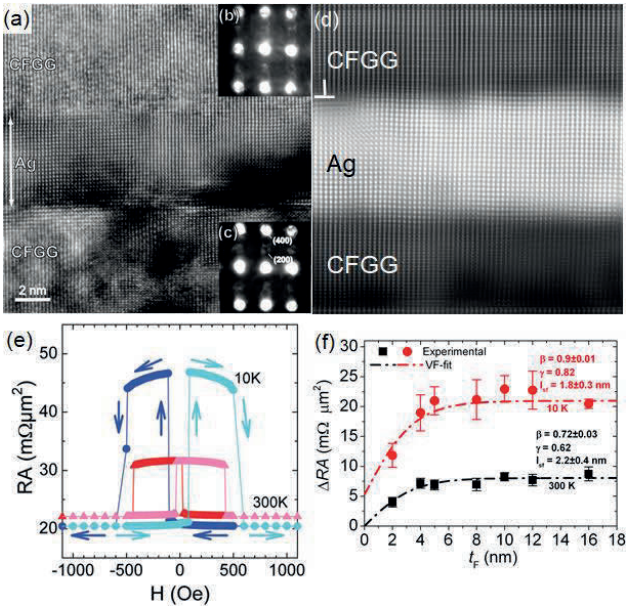

Fig. 16 (a) High-resolution TEM image of CFGG/Ag/CFGG. Nanobeam diffraction patterns are shown for (b) the top and (c) the bottom CFGG layers. (d) Cross-sectional HAADF-STEM image of CFGG/Ag/CFGG part in CPP-GMR device. (e) MR curves of CPP-GMR device with the CFGG(12)/Ag(5)/CFGG(12) at 10 K and 300 K. (f) change of ΔRA as a function of film thickness in CFGG at 10 K and 300 K. (Reproduced from *Appl. Phys. Lett.*, **98**, 152501 (2011) with permission of American Institute of Physics).

equation, it was found that the spin polarizations of CFGG at RT and 10 K were high at 72% and 90%, respectively. By inserting a thin NiAl layer at the CFGG/Ag interface, the ΔRA and MR ratios were found to be 31 mΩ·μm and 82% at RT, and 78 mΩ·μm and 285% at 10 K, respectively, the highest values in the world[64]. In polycrystalline CPP-GMR, which is essential for practical use, Nakatani *et al*. achieved a performance that meets the 5 Tbit/in^2 requirement[65].

To achieve a high density in the HDD, the total film thickness of the read sensor must be reduced, as shown in Figure 17. This is because the bit size of the medium decreases as the density increases, and in the case of 5 Tbit/in^2, it must be designed to be 13.5 nm or less[66]. In the case of a magnetoresistive element, the magnetization of one ferromagnetic electrode is fixed in one direction by an antiferromagnetic layer. Because the thickness of the antiferromagnetic layer is approximately 10 nm, it is difficult to reduce the overall thickness of the device to less than 13.5 nm. Conversely, as shown in Figure 17, non-local spin valve devices have only a free/nonmagnetic layer facing the medium and have the advantage of a greater degree of freedom in film thickness than magnetoresistive elements. To date, most research on non-local spin valve elements has focused on basic studies, such as spin current detection in non-local configurations, and not many of them have been aimed at HDD read device applications. Therefore, permalloy is a typical material considered a ferromagnetic electrode, and its spin signal is small. According to a one-dimensional spin diffusion model, the spin signal of

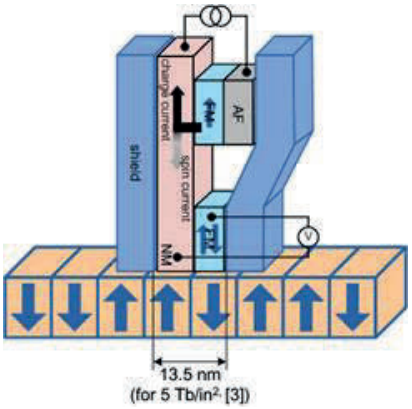

Fig. 17 Schematic image of read sensor using a non-local spin valve device. Since the spin injection and detection parts are laterally separated, the shield-to-shield gap, which corresponds to the head resolution, can be reduced dramatically. For 5 Tb/in^2, it should be less than 13.5 nm. (Reproduced from *Appl. Phys. Lett*., **100**, 052405 (2012) with permission of American Institute of Physics).

non-local spin valve devices can be increased by using ferromagnetic materials with high spin polarization and realizing high interface spin polarization. Non-local spin-valve devices were fabricated using CFGG, a highly spin-polarized material, to obtain a high-spin signal. Figure 18(a) shows an SEM image of the microfabricated device with two CFGG wires, both of which have a B2-ordered structure. Figure 18(b) shows a typical non-local magnetoresistance curve. The distance between the two CFGG wires in the device was 350 nm. High and low magnetoresistance correspond to the antiparallel and parallel configurations of the magnetization of the CFGG wires, respectively. A 12.8-mΩ spin signal (ΔR_s) was obtained, which was much higher than that of the permalloy (Py) and Cu lateral spin valve devices. ΔR_s was plotted against the distance between the CFGG wires and fitted to a one-dimensional spin diffusion model. The spin polarizations of 79% and 27% at the bulk and interface, respectively, are in good agreement with the estimated

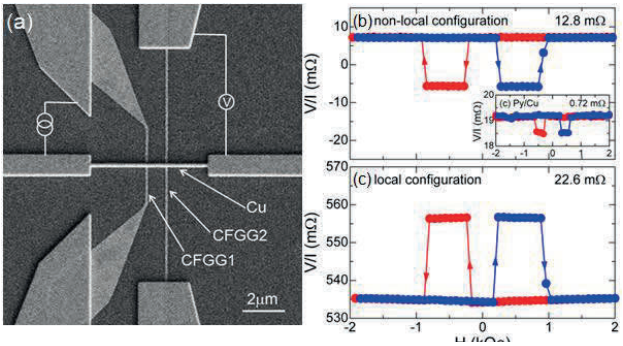

Fig. 18 (a) An SEM image of a typical non-local spin valve device using highly spin-polarized CFGG and Cu. (b) The spin signal in non-local configuration and (c) that in the local configuration as a function of the magnetic field in the CFGG/Cu non-local spin valve device. The inset shows the spin signal in the non-local configuration of the non-local spin valve device using Py and Cu. (Reproduced from *Appl. Phyhs. Lett*., **100**, 052405 (2012) with permission of American Institute of Physics).

values by the CPP-GMR devices. The lower spin polarization at the interface was probably due to the poor band matching of CFGG/Cu. As described above, success was achieved in obtaining high MR ratios and spin signals in CPP-GMR and non-local spin-valve devices using CFGG, a newly developed high-spin-polarization material.

3. Summary

Efforts to improve the properties of magnetic recording devices through microstructure control have been reviewed in this study. The microstructure plays a major role in the improvement of magnetic device characteristics. When the author began her career, the experimental technique of using TEM for microstructure observation as a tool for device development was uncommon. However, because the mechanism of property development can be well explained by observing microstructures, TEM is now one of the tools used for device development, and this research method is widely accepted. Although the microstructures can now be easily observed, their magnetic properties are not completely controlled. The high-speed operation of magnetic-recording devices will advance further in the future. To control the magnetic properties in the high-frequency range, it is necessary to understand the dynamic properties of magnetization.

Acknowledgements These studies were the result of working with many collaborators. The author would like to thank them for this opportunity, and especially Dr. Hono of NIMS, with whom they have worked with for many years.

References

1) M.N. Baibich, J.M. Broto, A. Fert, N.V. F. Dau, F. Petroff, P. Etienne, G. Creuzet, A. Friederich, J. Chazelas: *Phys. Rev. Lett*., **61**, 2472（1988）.
2) S. Iwasaki and Y. Nakamura: *IEEE Trans. Magn.,* **13**, 1272（1977）.
3) S. Yuasa, T. Nagahama, A. Fukushima, Y. Suzuki, K. Ando: *Nat. Mater*., **3**, 868（2004）.
4) S.S.P. Parkin, C. Kaiser, A. Panchula, P.M. Rice, B. Hughes, M. Samant, S-H. Yang: *Nat., Mater*. **3**, 862（2004）.
5) O.A. Ivanov, L.V. Solina, V.A. Demshima, L.M. Maget: *Phys. Met. Metallgr.,* **35**, 81 (1973).
6) H. Okamoto: Phase Diagram for Binary Alloys, p. 371（1995）
7) Y. Yasuda, N. Kimura, K. Hono, T. Sakurai, K. Yasuda: *J. Mang. Magn. Mater*., **170**, 289 (1997).
8) M. Watanabe, T. Masumoto, D.H. Ping, K. Hono: *Appl. Phys. Lett*., **76**, 3971 (2000).
9) A. Perumal, Y. K. Takahashi, K. Hono: *Appl. Phys. Express* **1**, 101301 (2008).
10) L. Zhang, Y.K. Takahashi, K. Hono, B.C. Stipe, J.-Y. Juang, M. Grobis: *J. Appl. Phys*.,**109**, 07B703 (2011).
11) L. Zhang, Y. K. Takahashi, K. Hono, B. C. Stipe, J.-Y. Juang, M. Grobis: *IEEE Trans. Magn.*,**47**, 4062 (2011).
12) B. S. D. Ch. S. Varaprasad, Y. K. Takahashi, J. Wang, T. Ina, T. Nakamura, W. Ueno, K. Nitta, T. Uruga, K. Hono: *Appl. Phys. Lett*., **104**, 222403 (2014).

13) I. Suzuki, J. Wang, Y.K.Takahashi, K. Hono: *J. Magn. Magn. Mater.*, **500**, 166418 (2020).
14) B. S. D. Ch. S. Varaprasad, J. Wang, T. Shiroyama, Y. K. Takahashi, K. Hono: *IEEE Trans. Magn*., **51**, 3200904 (2015).
15) B. S. D. Ch. S. Varaprasad, Y. K. Takahashi, A. Ajan, K. Hono: *J. Appl. Phys*., **113**, 203907 (2013).
16) J. Wang, H. Sepehri-Amin, H. Tajiri, T. Nakamura, K. Masuda, Y.K. Takahashi, T. Ina, T. Uruga, I. Suzuki, Y. Miura, K. Hono: *Acta Mater*., **166**, 413-423 (2019).
17) D. Weller: *IEEE Trans Magn*.,**50**.3100108 (2014).
18) I. Suzuki et al., to be submitted.
19) Y. K. Takahashi, T. Koyama, M. Ohnuma, T. Ohkubo, K. Hono: *J. Appl. Phys*., **95**, 2690 - 2696 (2004).
20) C. D. Stanciu, F. Hansteen, A. V. Kimel, A. Kirilyuk, A. Tsukamoto, A. Itoh, Th. Rasing: *Phys. Rev. Lett*.,**99**, 047601 (2007).
21) I. Radu, K.Vahaplar, C. Stamm, T.Kachel, N. Pontius, H.A.Durr, T.A. Ostler, J. Barker, R.F.L. Evans, R. W. Chantrell, A.Tsukamoto, A. Itoh, A. Kirilyuk, Th. Rasing, A.V. Kimel: *Nature*,**14**, 205 (2011).
22) A. Kirilyuk, A.V. Kimel, T. Rasing: *Rev. Mod. Phys*.,**82**, 2731 (2010).
23) A. R. Khorsand, M. Savoini, A. Kirilyuk, A. V. Kimel, A. Tsukamoto, A. Itoh, Th. Rasing: *Phys. Rev. Lett*.,**108**, 127205 (2012).
24) T. J. Huisman, R. V. Mikhaylovskiy, J. D. Costa, F. Freimuth, E. Paz, J. Ventura, P. P. Freitas, S. Blügel, Y. Mokrousov, Th. Rasing, A. V. Kimel: *Nat Nanotech.,***11**, 455, (2016).
25) S. Mangin, M. Gottwald, C-H. Lambert, D. Steil, V. Uhlíř, L. Pang, M. Hehn, S. Alebrand, M. Cinchetti, G. Malinowski, Y. Fainman, M. Aeschlimann, E. E. Fullerton: Nat. Mater., 13, 286 (2014).
26) C-H. Lambert, S. Mangin, B. S. D. Ch. S. Varaprasad, Y. K. Takahashi, M. Hehn, M. Cinchetti, G. Malinowski, K. Hono, Y. Fainman, M. Aeschlimann, E. E. Fullerton: *Science*, **345**, 1337 (2014). Y.K. Takahashi, R. Medapalli, S. Kasai, J. Wang, K. Ishioka, S.H. Wee, O. Hellwig, K. Hono, E.E. Fullerton: *Phys. Rev. Appl*., **6**, 054004 (2016).
27) M.S.El Hadri, P. Pirro, C.-H. Lambert, N. Bergeard, S. Petit-Watelot, M. Hehn, G. Malinowski, F. Montaigne, Y. Quessab, R. Medapalli, E. E. Fullerton, S. Mangin: *Appl. Phys. Lett*., **108**, 092405 (2016).
28) J. Wang, S. Sugimoto, S. Kasai, Y.K. Takahashi: *J. Phys.D:Applied Phys*.**53**, 475002 (2020).
35) Z. Gercsi and K. Hono: *J. Physics: Condensed Matter,* **19**, 326216 (2007).
36) B. S. D. Ch. S. Varaprasad, A. Rajanikanth, Y. K. Takahashi, K. Hono: *Appl. Phys. Express*., **3**, 023002 (2010).
37) B. Varaprasad, A. Rajanikanth, Y. K. Takahashi, K. Hono: *Acta Mater*., **57**, 2702-2709 (2009).
38-41) To be submitted.
42) A. Rajanikanth, Y.K. Takahashi, K. Hono: *J. Appl. Phys*., **103**, 103904 (2008).
43-45) To be submitted.
45) S. V. Karthik, A. Rajanikanth, T. M. Nakatani, Z. Gercsi, Y. K. Takahashi, T. Furubayashi, K. Inomata, K. Hono: *J. Appl. Phys.*, **102**, 043903 (2007).
46) To be submitted.
47) A. Rajanikanth, D. Kande , Y.K. Takahashi, K Hono: *J. Appl. Phys.*, **101**, 09J508 (2007).
48-51) To be submitted.
52) S. V. Karthink, A. Rajanikanth, Y. K. Takahashi, T. Ohkubo, K. Hono: *Appl. Phys. Lett.,* **89**, 052505 (2006).
53,54) To be submitted.
55) A. Rajanikanth, Y. K. Takanashi and K. Hono: *J. Appl. Phys.,* **105**, 063916 (2009).
56) To be submitted.
57) T. M. Nakatani, Z. Gercsi, A. Rajanikanth, Y. K. Takahashi, K. Hono: *J. Phys. D: Applied Physics.*, **41** 225002 (2008).
58) To be submitted.
59) S. V. Karthik, A. Rajanikanth, Y. K. Takahashi, T. Okhubo, K. Hono: *Acta Mater.,* **55**, 3867 - 3874 (2007).
60) A. Narahara, K. Ito, T. Suemasu, Y. K. Takahashi, A. Rajanikanth, K. Hono: *Appl. Phys. Lett.,* **94**, 202502 (2009).
61) A. Rajanikanth, S. Kasai, N. Ohshima, K. Hono: *Appl. Phys. Lett*., **97**, 022505 (2010)
62) Y.K. Takahashi, A. Srinivasan, B. Varaprasad, A. Rajanikanth, N. Hase, T.M. Nakatani, S. Kasai, T. Furubayashi, K. Hono: *Appl. Phys. Lett*., **98**, 152501 (2011).
63) Y. K. Takahashi, S. Kasai, S. Hirayama, S. Mitani, K. Hono: *Appl. Phys. Lett*., **100**, 052405 (2012).
64) J. W. Jung, Y. Sakuraba T. T. Sasak, Y. Miura, K. Hono: *Appl. Phys. Lett*. **108**, 102408 (2016).
65) T. Nakatani, T. T. Sasaki , Y. Sakuraba, K. Hono: *J. Appl. Phys*., **126**, 173904 (2019).
66) M. Takagishi, K. Yamada, H. Iwasaki, H. N. Fuke, S. Hashimoto: *IEEE Trans. Magn.,* **46**, 2086 (2010).

Received 29. April, 2022; Accepted 20. May, 2022

J. Magn. Soc. Jpn., **46**, 85-89 (2022)

<Paper>

A correction of measurement for complex magnetic permeability by direct contact probe

Z. Wang, T. Ishihara, K. Okita*, S. Yabukami*

Graduate school of Engineering, Tohoku Univ., *6-6-05 Aramaki aza-aoba, Aoba-ku, Sendai 980-8579, Japan*

*Graduate school of Biomedical Engineering, Tohoku Univ., *6-6-05 Aramaki aza-aoba, Aoba-ku, Sendai 980-8579, Japan*

A method for obtaining magnetic permeability of thin film by the direct contact probe was developed and the measurement error of permeability was reduced. We analyzed the frequency dependence of a current path inside the magnetic thin film using by finite element method. The magnetic permeability was corrected in consideration of the frequency dependence of the high-frequency current inside the magnetic thin film. The permeability of CoNbZr film (5 mm x 5 mm, 2 μm in thickness) was optimized by the method, and measured permeability was roughly agreed with the theoretical value up to 4 GHz.

Key words: Complex permeability, Direct contact probe, Current path

1. Introduction

The need to evaluate the high-frequency permeability of magnetic thin films has increased because of high-frequency fifth-generation, spintronic devices, etc. Several methods have been reported for evaluating the high-frequency magnetic permeability of magnetic materials and thin films [1)-5)]. In addition, highly sensitive methods for evaluating thin film with a thickness of several nm are expected. A method for obtaining magnetic permeability of thin film by the direct contact probe was developed in our previous research [6)]. However, ignoring the current concentration due to the skin effect on the sides of the magnetic thin film, the real part of permeability in the low-frequency band showed a tendency to decrease, and it does not correspond to the theoretical value of permeability. In the present study, we analyzed the frequency dependence of a high-frequency current path inside the magnetic thin film using by finite element method. Since a high-frequency current flows directly through the magnetic film and the impedance at that time is measured to calculate the magnetic permeability, it is necessary to analyze the high-frequency current distribution in the magnetic film and reflect it in the impedance measurement results. We correct the measurement error of permeability in the low-frequency range and accurately evaluate CoNbZr film's permeability.

2. Experiment method and procedure

Fig. 1 (a), Fig. 1 (b) and Fig 1. (c) present views of the probe. Fig. 2 shows a photograph of the appearance of the probe connected to the magnetic thin film. The probe comprises a microstrip conductor on a substrate and the ground plane which made by copper and two connectors. We use two SMA connectors (CON-SMA-EDGE-S RS) to measure high-frequency response. The center pin of the

Corresponding author: Ziyuan Wang (e-mail: wesleyinter620@gmail.com).

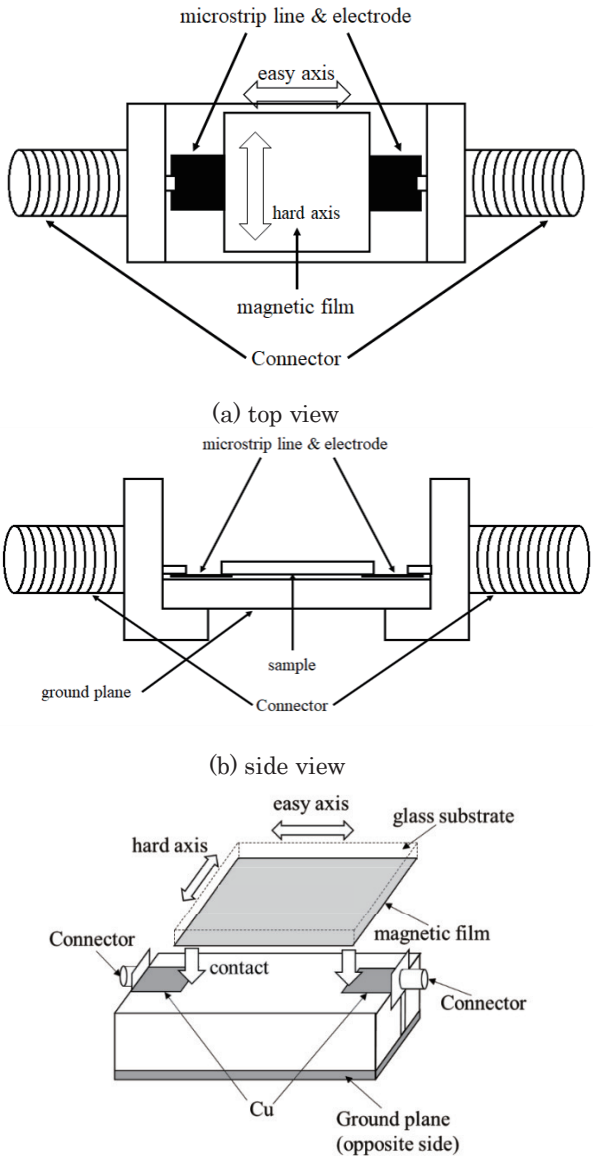

Fig. 1 View of the probe.

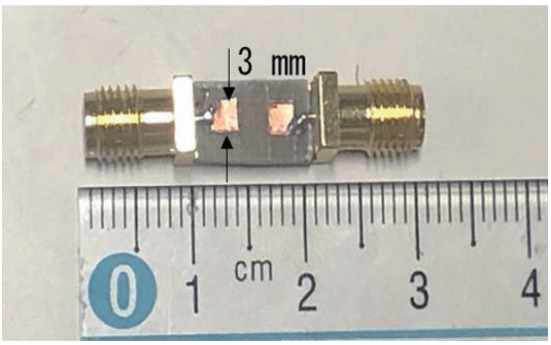

Fig. 2 Photograph of the probe.

connector was connected to a microstrip line which made of copper and fixed by solder. The microstrip conductors of the probe were contacted with the magnetic thin film (CoNbZr film). Therefore, the high-frequency current flows from the microstrip line to the magnetic thin film directly.

Coaxial cables are connected to a network analyzer (R3767CG; Advantest Inc.) and a PC was connected to the network analyzer to control the measurement setting. The flow chart of this experiment is shown in Fig. 3. The transmission coefficient (S_{21}) is calibrated by application of a strong DC field (approx. 397.9 kA/m; 5 k Oe) in the direction of the easy axis to saturate the magnetic thin film. Secondly, S_{21} is measured with 10 Oe (795.77 A/m), 30 Oe (2387.32 A/m), and 50 Oe (3978.87 A/m) DC fields. The complex impedance Z_s is calculated from S_{21} by the following equation [5].

$$Z_S = \frac{2Z_0(1-S_{21})}{S_{21}} \quad (1)$$

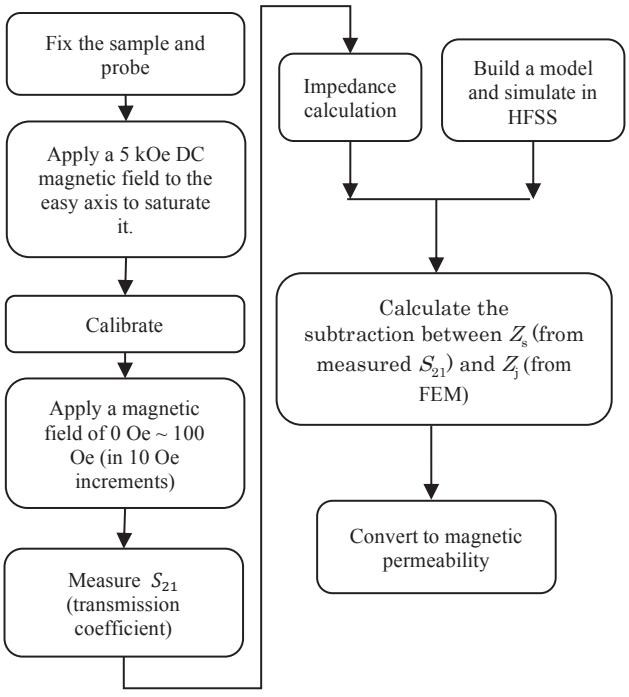

Fig. 3 The flow chart of this experiment.

where Z_0 is the characteristic impedance and is about 50 Ω.

The real part of relative permeability is proportional to reactance and the imaginary part is proportional to resistance.

$$\mu_r' \propto X/f \quad (2)$$

$$\mu_r'' \propto R/f \quad (3)$$

We focused on the frequency dependence of the current path as a factor of error. This part will introduce the calculation method of the impedance Z_j, which is obtained from the FEM analysis considering the localization of the current path. Z_j was calculated according to the above calculation method by using the S_{21} parameter and equation (1). Z_j was obtained from the FEM with μ_r= 1 in Fig. 3.

3. Experiment results

3.1 Preliminary experiment

We prepared a CoNbZr thin film (5 mm × 5 mm, 2 μm thickness). The magnetic thin film was made by a sputtering system and the magnetic anisotropy was applied by a magnetic annealing machine. Fig. 4 shows the MH curve of the CoNbZr thin film measured by a VSM. The anisotropy field around 9 Oe (716.22 A/m) was evaluated.

Fig. 5 shows the measurement results of impedance of CoNbZr thin film and the impedance can be calculated by equation (1).

Fig. 6 shows the real part of permeability of CoNbZr thin film obtained by a method that does not consider the concentration of the current to the side edge of the magnetic thin film. The real part of magnetic permeability shows a tendency to decrease, and it does not correspond to the theoretical value of permeability.

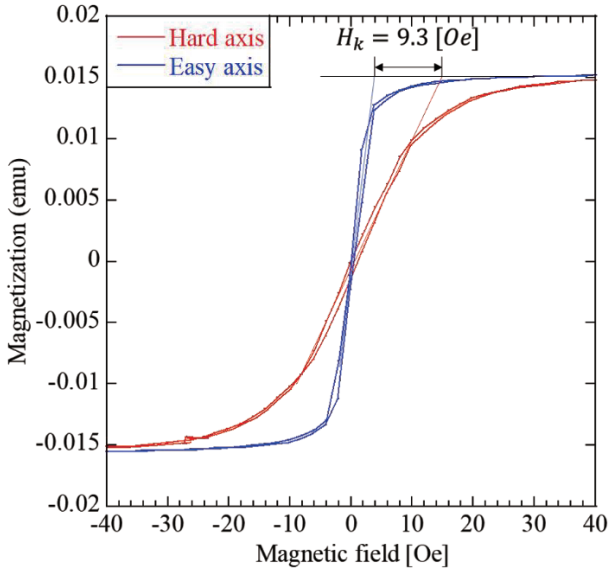

Fig. 4 The MH curve of the CoNbZr thin film.

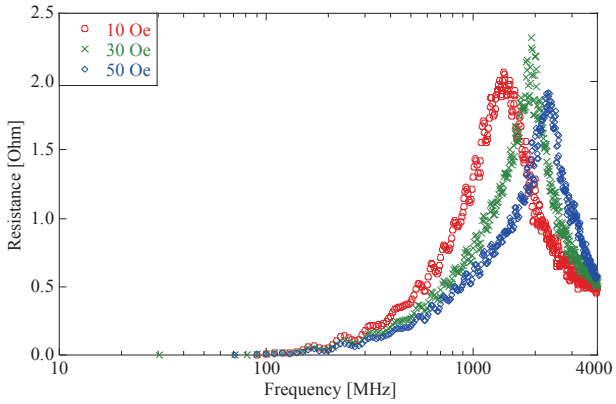

(a) Resistance of the magnetic film

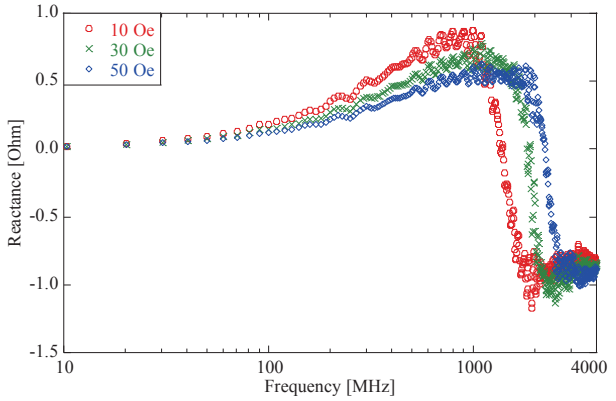

(b) Reactance of the magnetic film

Fig. 5 measurement results of impedance of CoNbZr thin film.

Therefore, we realized there was a measurement error, especially in a low-frequency range.

3.2 FEM analysis

Next, we established a model in HFSS (ANSYS Corp.) to analyze the current distribution using the finite element method. The model is shown in Fig. 7 and it is identical to the original probe. The electromagnetic field analysis in HFSS was performed by setting the relative permeability of the magnetic thin film to 1 and 1000,

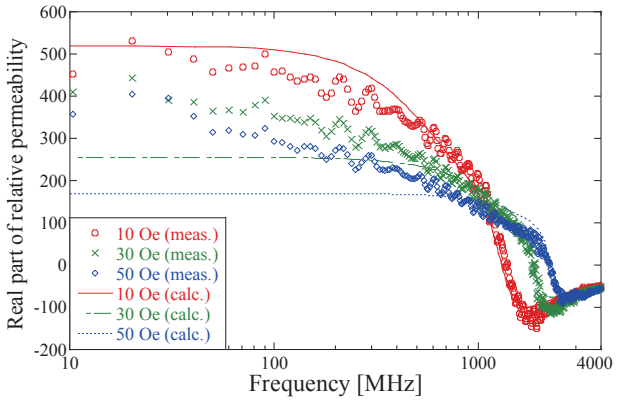

Fig. 6 The real part of complex permeability of CoNbZr film (2 μm thick).

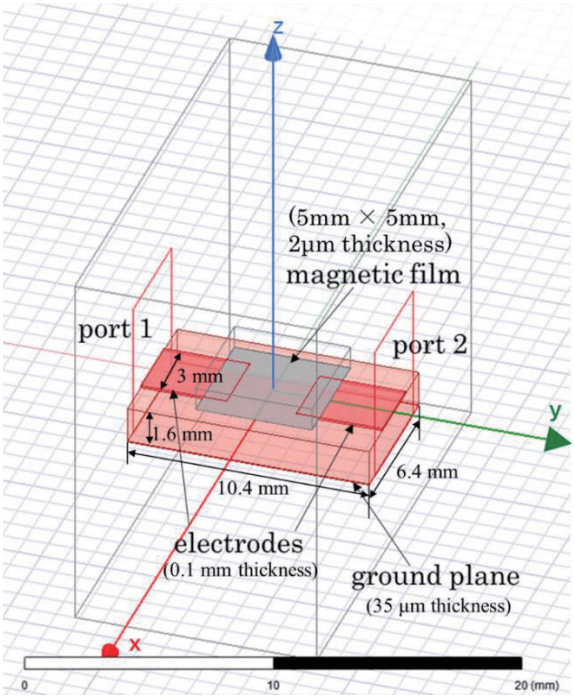

Fig. 7 The analysis model in HFSS.

respectively, and the conductivity of the magnetic thin film was set as 8×10^5 S/m. The material of the ground conductor and electrodes were set as copper. The outer part is the air that is the environment. The boundary condition is radiation for all parts that are not ports. The left and right rectangles are the ports, set as Wave port and input 1 mW of electric power. HFSS repeats mesh subdivision and electromagnetic field analysis. Mesh generation will complete when the change of S parameter becomes small enough. If a sufficiently fine mesh is obtained, the S parameter between Passes will be stable and $S^{N+1} \approx S^N$ is satisfied. Where the N is the number of analyzes. Therefore, if the reference value Maximum ΔS is determined and the convergence condition Maximum $\Delta S > S^{N+1} - S^N$ is satisfied, it is judged that the optimum mesh is obtained. So, to ensure the calculation accuracy of the FEM analysis, the ΔS is set to very small (ΔS <0.0001) and the number of calculation elements is also very large (about 3×10^6). On the other hand, to ensure the calculation speed, the number of frequency points is not very large.

Fig. 8 (a) and Fig. 8 (b) present the current distribution on the magnetic thin film and the frequency is 10 MHz and 1 GHz, respectively. The current on the surface of the magnetic thin film is represented by vectors and Fig. 9 graphs the current distribution on the surface of the magnetic thin film on the central axis. It was found that the current distribution gradually localized at the edge as the frequency increased. The current path has become narrower. So, it is cognized that the error factor is the current path in the magnetic thin film.

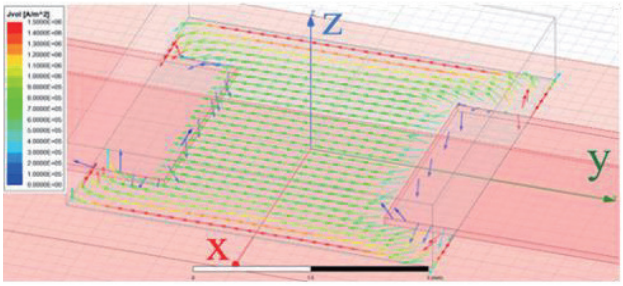

(a) When the frequency is 1 GHz

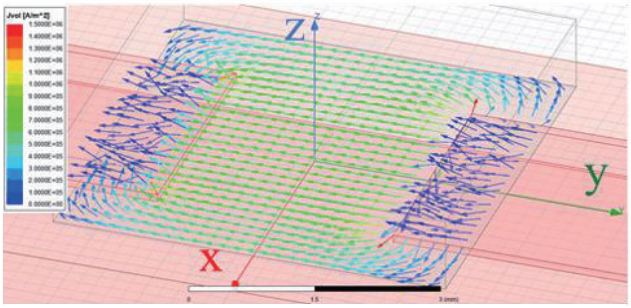

(b) When the frequency is 10 MHz

Fig. 8 Current distribution on the magnetic film.

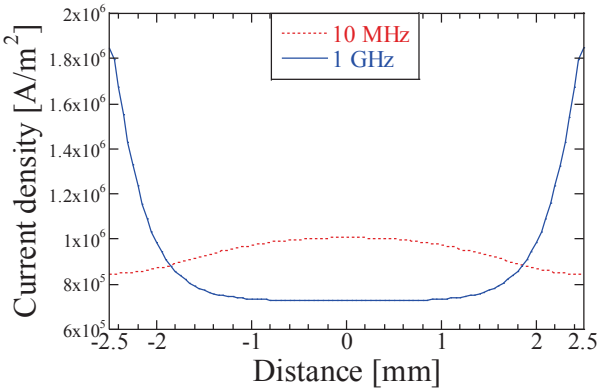

Fig. 9 Current distribution on the central axis.

3.3 Correction Method

Then from the Z-parameter measurement function, assuming the circuit of the measurement system is a T-type circuit, as shown as Fig. 10, the Z matrix is [7]

$$Z = \begin{bmatrix} Z_{11} & Z_{21} \\ Z_{12} & Z_{22} \end{bmatrix} = \begin{bmatrix} Z_j/2 + 1/Y_j & 1/Y_j \\ 1/Y_j & Z_j/2 + 1/Y_j \end{bmatrix} \quad (4)$$

and the impedance of magnetic film is

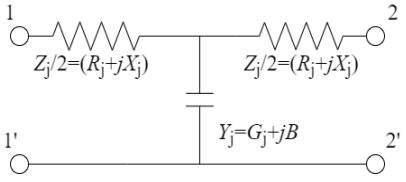

Fig. 10 T-type equivalent circuit.

$$Z_j = Z_{11} + Z_{22} - 2Z_{21} \quad (5).$$

We calculated the impedance corresponding to the two permeability and their subtraction Z_j was obtained. After that, with the subtraction between Z_s (from measured S_{21}) and Z_j (from FEM), we can eliminate the error of the current localization.

Fig. 11 (a) shows the calculated resistance, R_j, and reactance, X_j, and (b) shows conductance, G_j, and susceptance, B_j as a function of frequency. These values are obtained by equation (4) and (5). Impedance are critical for the obtaining magnetic permeability.

The real part of permeability before the correction is compared with the FEM analysis in Fig. 12. Simulated results are obtained from S_{21} of HFSS and equation (1)-(3). These results show the real part of permeability

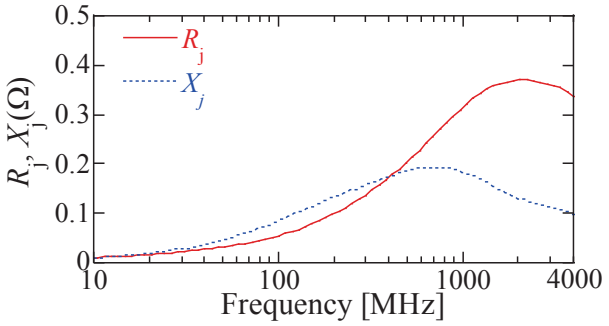

(a) The calculated impendance, R_j, X_j

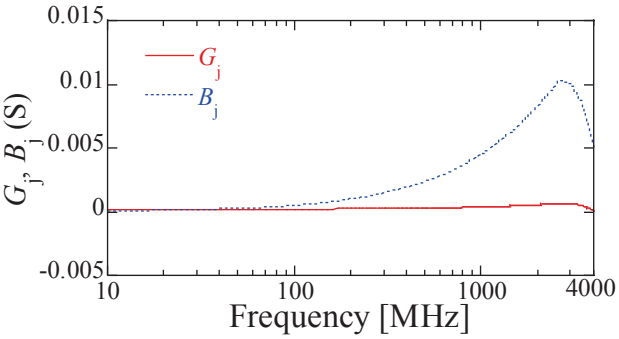

(b) The calculated admitance, G_j, B_j

Fig. 11 Calculation result from FEM analysis.

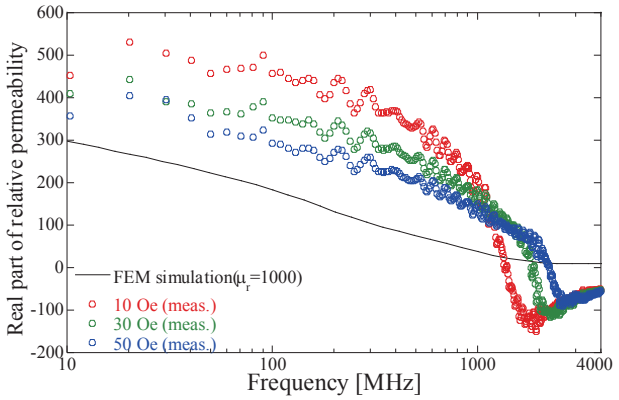

Fig. 12 Real part of permeability of CoNbZr film (2 μm thick) before a correction and after FEM simulation.

decreased as frequency increased because the high-frequency current gradually localized at the edge of the magnetic thin film as frequency increased. At low frequencies, the slope of the gradual decrease in the real part of magnetic permeability almost matches the calculated value of FEM, therefore the effect of current localization is dominant.

4. Correction Results

Fig. 13 shows the corrected measurement result of the hard axis real part of permeability of CoNbZr film (5 mm × 5 mm, 2 μm thickness) by calculating the subtraction. The symbols show measured permeability, and the dotted lines and the solid lines show the theoretical permeability based on the Landau–Lifshitz–Gilbert equation and eddy current generation [8], respectively. A g factor of 2.13 was used to calculate theoretical permeability. An α (damping factor) of 0.02 was used to fit theoretical permeability to measured spectra. The absolute permeability was calibrated by the application of dc magnetic fields in the direction of the easy axis [8]. The DC bias field of 10 Oe (795.77 A/m), 30 Oe (2387.32 A/m), and 50 Oe (3978.87 A/m) was applied to the hard axis. The measured magnetic permeability corresponds to the theoretical value obtained by the LLG equation and eddy current generation [8], and the real part of magnetic permeability is close to constant in low frequency. Since the difference in the current path between the background measurement (strong DC field application along to easy axis) and the main measurement is more significant at lower frequencies, the effect of correction is more dominant at lower frequencies. From Fig. 11 and Fig. 12, the correction seems to be large for the stronger magnetic field (50 Oe) in the low-frequency band. This is because the current localization is more dominant in the low-frequency band, and the decrease of magnetic permeability in the correction is more prominent as the magnetic permeability is lower.

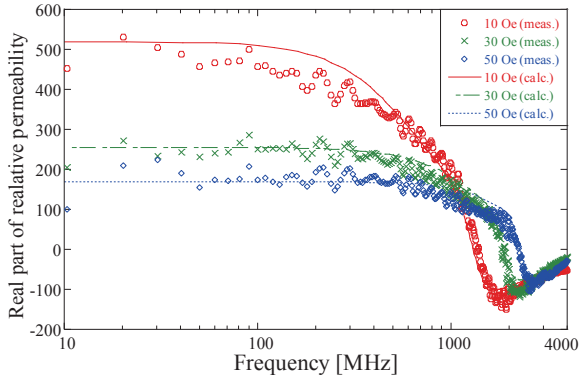

(a) Real part of relative permeability

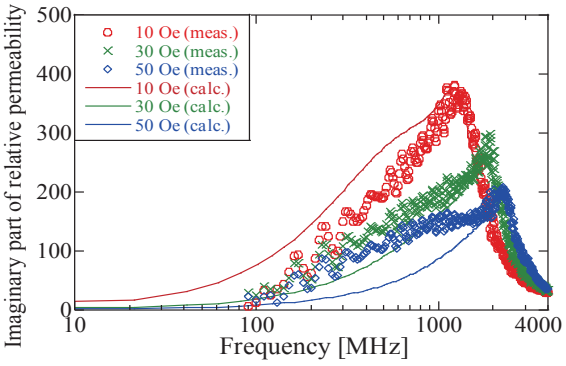

(b) Imaginary part of relative permeability

Fig. 13 Calculation result after the subtraction.

5. Conclusion

1. We fabricated a direct contact probe for evaluating thin-film permeability and reduce the permeability measurement error.
2. We analyzed the frequency dependence of a current path inside the magnetic thin film using by finite element method and found that the measurement error of low-frequency magnetic permeability is caused by the fact that the current path changes greatly depending on the frequency.
3. The magnetic permeability was corrected in consideration of the frequency dependence of the high-frequency current inside the magnetic thin film and the permeability of CoNbZr film (5 mm x 5 mm, 2 μm in thickness) was measured accurately up to 4 GHz.

Acknowledgments This work was supported in part by the Business Incubation Program (BIP) of Tohoku University, research and development for expansion of radio wave resources from the Ministry of Internal Affairs and Communications (JPJ000254), KIOXIA Corporation, and NEDO Entrepreneurs Program (0329006).

References

1) P. A. Calcagno and D. A. Thompson, *Rev. Sci. Instrum.*, **46**, 904 (1975).
2) M. Yamaguchi, S. Yabukami, and K. I. Arai, *IEEE Trans. Magn.*, **32**, 4941 (1996).
3) H. B. Weir, *Proc IEEE*, **62**, 33 (1975).
4) A. M. Nicolson and G. F. Ross, *IEEE Trans. Instrum. Meas.*, **19**, 377–382 (1970).
5) S. Yabukami, K. Nozawa, L. Tonthat, K. Okita, and S. Ranajit, *IEEE Trans. Magn.*, **56**, 6100405 (2020).
6) S. Yabukami: "Measurement of thin film permeability by direct contact and optimization", *J. Appl. Phys.*, **105**, 07E719 (2009).
7) A. Smith, "Radio Frequency Principles and Applications,"**157**, (IEEE Press, New York, 1998).
8) Y. Shimada, J. Numazawa, Y. Yoneda and A. Hosono: *J. Magn. Soc. Jpn.*, **15**, 327 (1991).

Received Jan. 15, 2022; Revised Apr. 13, 2022; Accepted Apr. 30, 2022

Journal of the Magnetics Society of Japan

Vol. 46 No. 4 (通巻第322号) 2022年7月1日発行

Vol. 46 No. 4 Published Jul. 1, 2022
by the Magnetics Society of Japan
Tokyo YWCA building Rm207, 1–8–11 Kanda surugadai, Chiyoda-ku, Tokyo 101–0062
Tel. +81–3–5281–0106 Fax. +81–3–5281–0107

Printed by JP Corporation Co., Ltd.
Sports Plaza building 401, 2–4–3, Shinkamata Ota-ku, Tokyo 144–0054
Advertising agency: Kagaku Gijutsu-sha

発行：（公社）日本磁気学会 101–0062 東京都千代田区神田駿河台 1–8–11 東京YWCA会館 207 号室
製作：ジェイピーシー 144–0054 東京都大田区新蒲田 2–4–3 スポーツプラザビル401 Tel.（03）6715–7915
広告取扱い：科学技術社 111–0052 東京都台東区柳橋 2–10–8 武田ビル 4F Tel.（03）5809–1132